




Effect of Mn Addition on Melt Purification and Fe Tolerance in Mg Alloys

TAO CHEN,¹ YUAN YUAN ^{1,5,6} TINGTING LIU,² DAJIAN LI,³
AITAO TANG,¹ XIANHUA CHEN,¹ RAINER SCHMID-FETZER,⁴
and FUSHENG PAN¹

1.—National Engineering Research Center for Magnesium Alloys, College of Materials Science and Engineering, Chongqing University, Chongqing 400000, People's Republic of China. 2.—Faculty of Materials and Energy, Southwest University, Chongqing 400715, People's Republic of China. 3.—Institute for Applied Materials – Applied Materials Physics (IAM-AWP), Karlsruhe Institute of Technology, D-76344 Karlsruhe, Germany. 4.—Institute of Metallurgy, Clausthal University of Technology, D-76344 Clausthal-Zellerfeld, Germany. 5.—e-mail: yuanyuan17@cqu.edu.cn. 6.—e-mail: yuan.yuan.er@gmail.com

Two methods for impeding the detrimental impact of iron (Fe) impurity in magnesium (Mg) alloys on the corrosion properties are studied: the addition of manganese (Mn) and the selection of melting temperature. Experimental work was carried out on Mg and AZ91 alloys with selected additions of Mn and selected settling temperatures. The settling velocity was evaluated using the Stokes equation. Extensive thermodynamic calculations using different databases in comparison were performed and supported by experimental observations. The conditions for the formation of the different types of precipitate phases and their detailed composition are revealed. Practical guidelines for settling temperature and time are proposed. The tolerance limit of Fe, expressed by the critical Fe/Mn ratio, could be related to key phase boundaries in the calculated Mg-Aluminum (Al)-(Zn)-Mn-Fe phase diagrams for AM and AZ types of alloys.

INTRODUCTION

As the lightest structural metallic materials, magnesium (Mg) alloys have attracted extensive attention, especially in the transportation field for energy saving and environment protection.^{1–5} However, their broad application is limited due to their natively poor anti-corrosion property. Mg has the lowest standard chemical potential among the common structural metals. Many types of precipitates in Mg alloys can cause severe galvanic corrosion in the service period.^{6,7} Especially, impurities like iron (Fe), nickel (Ni), copper (Cu), and cobalt (Co), with a quite small solubility in the α (Mg) phase (in ppm or 10 ppm range, ppm = mg/kg) and high chemical potential, were reported to severely deteriorate the corrosion resistance property of Mg alloys.^{7–10} Hence, many studies have been devoted to decrease

the content of these impurities during the alloy synthesis process and maximize the purity of the final Mg alloys.^{11–18}

Among these impurities, Fe, which is easily picked up during the synthesis of Mg alloys, is of key relevance.^{12,18–21} Iron is difficult to be completely avoided in the current production process of Mg alloys. Firstly, both melting crucibles and instruments are usually made from Fe-containing alloys.^{21,22} Secondly, most master alloys contain Fe impurities. Therefore, reducing the content of Fe and purifying the Mg alloys is always necessary to improve the corrosion resistance of Mg alloys. For example, manganese (Mn) additive is known to be able to effectively reduce Fe content to a certain limit in aluminum (Al)-containing Mg alloys, and zirconium (Zr) additive has been reported to be able to effectively reduce Fe content in Al-free Mg alloys.^{18,20,23–25} The effect of Zr addition is due to the formation of high-density Fe₂Zr compounds which readily settle to the bottom to be removed

during the settling process.²⁰ However, the mechanism of the Mn addition effect on Al-containing Mg alloys is more complicated and not theoretically clarified. In addition, there is no theoretically founded prediction of the advisable amount of the main addition in various Mg alloys.

Another important feature of galvanic corrosion of Mg alloys is that a tolerance limit value for impurities exists, which means that the corrosion rate will sharply increase when the impurity content is above a certain value.^{14,26–30} Accordingly, extending the tolerance limit of the impurities is a promising and practical approach to improve the corrosion resistance. Besides its purification effect, Mn is also experimentally observed to be a promising additive for increasing the tolerance limit of Fe in Al-containing Mg alloys. Specifically, a relationship between the tolerance limit of Fe and the Mn content in certain alloys has been experimentally reported.^{8,14,16,27,28,30} Hillis and Reichel²⁸ suggested that the tolerance limit of Fe might be correlated to a phase boundary in these systems. However, no theoretical or experimental evidence has been provided in the literature.

The CALPHAD (Computer Coupling of Phase Diagrams and Thermochemistry) approach^{21,31–34} integrated with the first-principles method^{35–37} and key experiments can provide theoretical descriptions and predictions of the elements' distribution and transformation in alloys. The purpose of this work is to investigate the effect of Mn addition on the purification and tolerance of Fe in Mg and its alloys by combining thermodynamic predictions and experiments. More specifically, Mg-Al-based AZ and AM series alloys (Mg-Al-Mn-Zn-Fe system) have been studied in the current work, since these are the dominant Mg alloy series.

STUDY METHODS

Twelve Mg alloys were synthesized by a resistance furnace under the protection of a mixed gas of 99.5 vol.% CO₂ and 0.5 vol.% SF₆. The detailed chemical compositions of the alloys and methods are given in Table S-I (Supplementary material). After the alloy had melted, the melt was kept at a certain temperature for 60 min and a small amount of alloy was sampled using copper tubes. The chemical analysis of these samples was analyzed by inductively coupled plasma optical emission spectrometry (Optima 8000). An amount of melt at the bottom was also taken by copper tubes for precipitate characterization using a scanning electron microscope (SEM) with energy-dispersive x-ray spectroscopy. The settling efficiencies of the second phases were evaluated using the Stokes law and the details are shown in Table S-II (Supplementary material). Pandat software (database of PanMg2013³³) and Thermo-Calc 2019a (database of TCMG5³⁸) were applied for the thermodynamic calculations.

RESULTS

Effect of Mn Addition on the Fe Distribution in Mg-(Fe) Melts

The calculated and experimentally measured Fe contents in Mg alloys with different Mn additions are listed in Table I. As shown in Fig. 1a, the eutectic liquid point of a Mg-Fe system is at 179 ppm Fe and 650°C, corresponding to the maximum solubility of Fe in Mg-melt at 650°C. Scepanovic et al.³⁹ measured the solubility of Fe in α (Mg) using a metallography method, and the solid solubility was proposed to be approximately 28 ppm at 500°C according to electron probe micro-analysis results. The current calculation shows that the solubility of Fe in α (Mg) is 10 ppm at the eutectic temperature. With 0.5 wt.% Mn addition, the liquid composition at the eutectic is reduced to 130 ppm Fe, and face-centered cubic (Fcc), denoted as Fcc(Fe, Mn) is precipitated, as shown in Fig. 1b. [The majority component in phases is shown in bold and the detailed descriptions of all phases in this work have been listed in Table S-III (Supplementary material)]. The calculated isothermal section of Mg-xMn-yFe at the settling temperature of 660°C in the Mg-rich corner is shown in Fig. 1c. The relationship of the joint solubility of Fe and Mn in liquid Mg, shown by the dotted line, is roughly linear at 660°C. The experiments also verified that the Fe content of the as-cast alloy can be controlled by the (initial) Mn-addition, as shown in Table I. Its value before settling is around 180 ppm according to our analysis of several samples. The Fe content was reduced to 100 ppm Fe with 0.5 wt.% Mn addition and to 66 ppm Fe with 1.5 wt.% Mn addition.

It has been observed that the Mn addition also changes the type of the precipitate phases. As shown in Fig. 1a, for Mg-Fe system, body-centered cubic (Fe) (Bcc(Fe)) is formed as the only precipitate. With the Mn addition, hypereutectic liquid precipitates Fcc(Fe, Mn) or complex body-centered cubic(Mn, Fe) (Cbcc(Mn, Fe)) are formed at 660°C, as shown in Fig. 1b and c. Here, the density and the further terminal settling velocities of these precipitates are similar to each other, hence, in this case, the type of the primary-precipitates does not have a significant impact on the settling process (see Table I).

Effect of Mn Addition on the Fe Distribution in Mg-Al-(Fe) Melts

The phase transformations of AZ series alloys from the liquid state to the solid state were also analyzed. A high initial contamination of 1000 ppm Fe is assumed for convenience, as any value above the low solubility limit provides qualitatively similar results. Starting with AZ91 (Mg-9Al0.7Zn0.1Fe, wt.%), the effect of adding 0.2 wt.% Mn, as shown in Fig. 2, was calculated in comparison with the mass phase fractions of AZ91(0Mn) and AZ91(0.2Mn).

Table I. Fe content and precipitates in saturated Mg-(180 ppm Fe) and Mg-xMn-(180 ppm Fe) alloys; comparison of Pandat-calculated and experimental data of this work

Alloy with 180 ppm Fe (Mn wt.%)	with T (°C)	Calc. Fe in liquid ^a (ppm)	Exp. Fe content ^b (ppm)	Precipitate phase ^c	Precipitate compos. ^d (wt.%)	Density ρ_{part} ($\times 10^3 \text{ kg/m}^3$)	v (m/s)
Mg	660	202	–	Bcc(Fe)	100Fe	7.9	1.6×10^{-4}
	650	179	–	Bcc(Fe)	100Fe	7.9	1.6×10^{-4}
Mg-0.5Mn	660	149	100	Fcc(Fe, Mn)	70Fe30Mn	7.7	1.5×10^{-4}
	650	130	100	Fcc(Fe, Mn)	69Fe31Mn	7.6	1.5×10^{-4}
Mg-1.5Mn	660	46	66	Cbcc(Mn, Fe)	78Mn22Fe	7.6	1.5×10^{-4}
	650	35	66		80Mn20Fe		
Mg-2Mn	660	13	12	Cbcc(Mn, Fe)	92Mn8Fe	7.6	1.5×10^{-4}
	650	9	12		93Mn7Fe		

ppm mg/kg, v settling velocity calculated using Stokes equation. ^aCalculated Fe content in equilibrated Liquid. ^bExperimentally measured Fe content in the as-cast alloy after settling. ^cCalculated solid phase type in equilibrium with Liquid, supported by SEM/EDS data. ^dCalculated solid phase composition in equilibrium with Liquid, supported by SEM/EDS data.

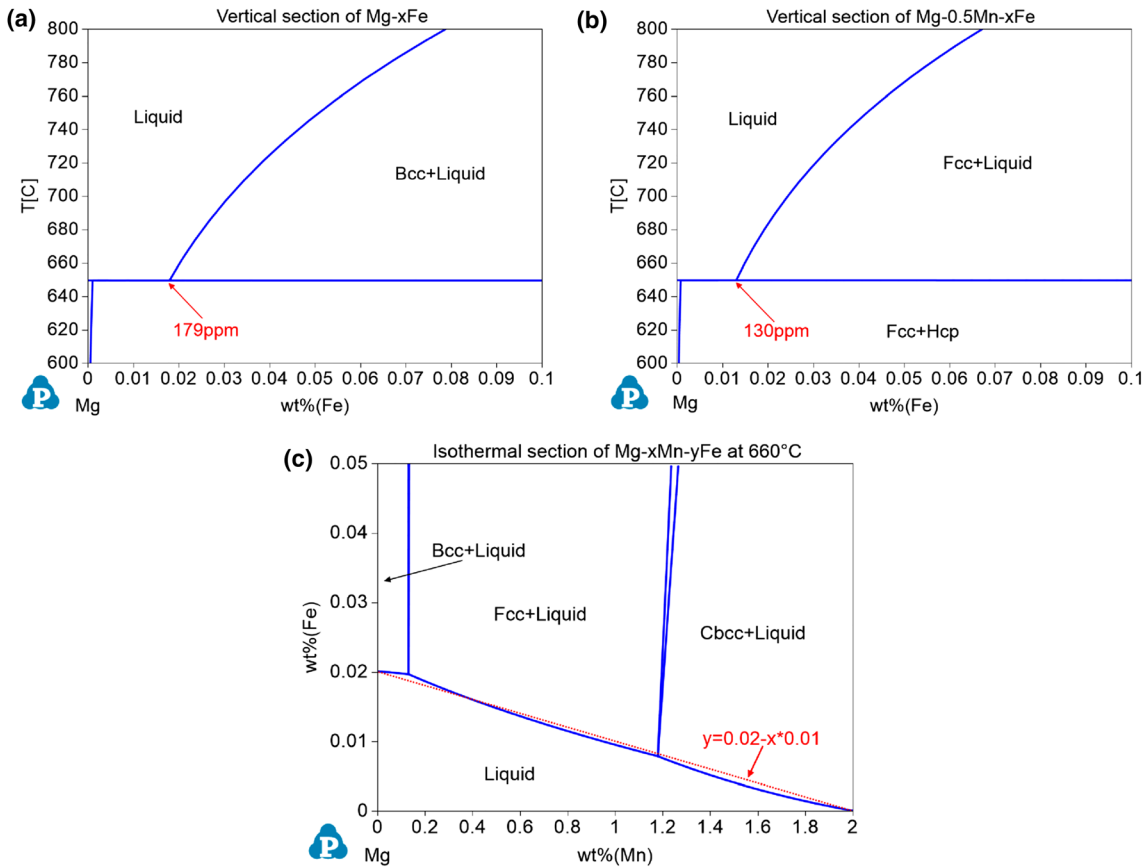


Fig. 1. (a) Calculated Mg-Fe phase diagram; (b) calculated isopleth of Mg-0.5Mn-xFe; (c) calculated isothermal section of Mg-xMn-yFe at 660°C.

The same calculations using TCMG and PanMg were performed, as shown in Fig. 2a, b, c, and d. Qualitatively similar results concerning the key point of the reduced formation temperature of Bcc and the occurrence of Al_3Mn_5 are obtained, even though quantitatively significant differences are

noted. Without Mn addition, the first precipitate that forms is Al_5Fe_2 , transforming to Al_2Fe upon heating, while the Fe-rich Bcc(Fe, Al), actually Bcc_B2, forms only above 760°C. With 0.2 wt.% Mn addition, the formation temperature of Bcc(Fe, Al, Mn) is reduced to 650°C, reaching a maximum at

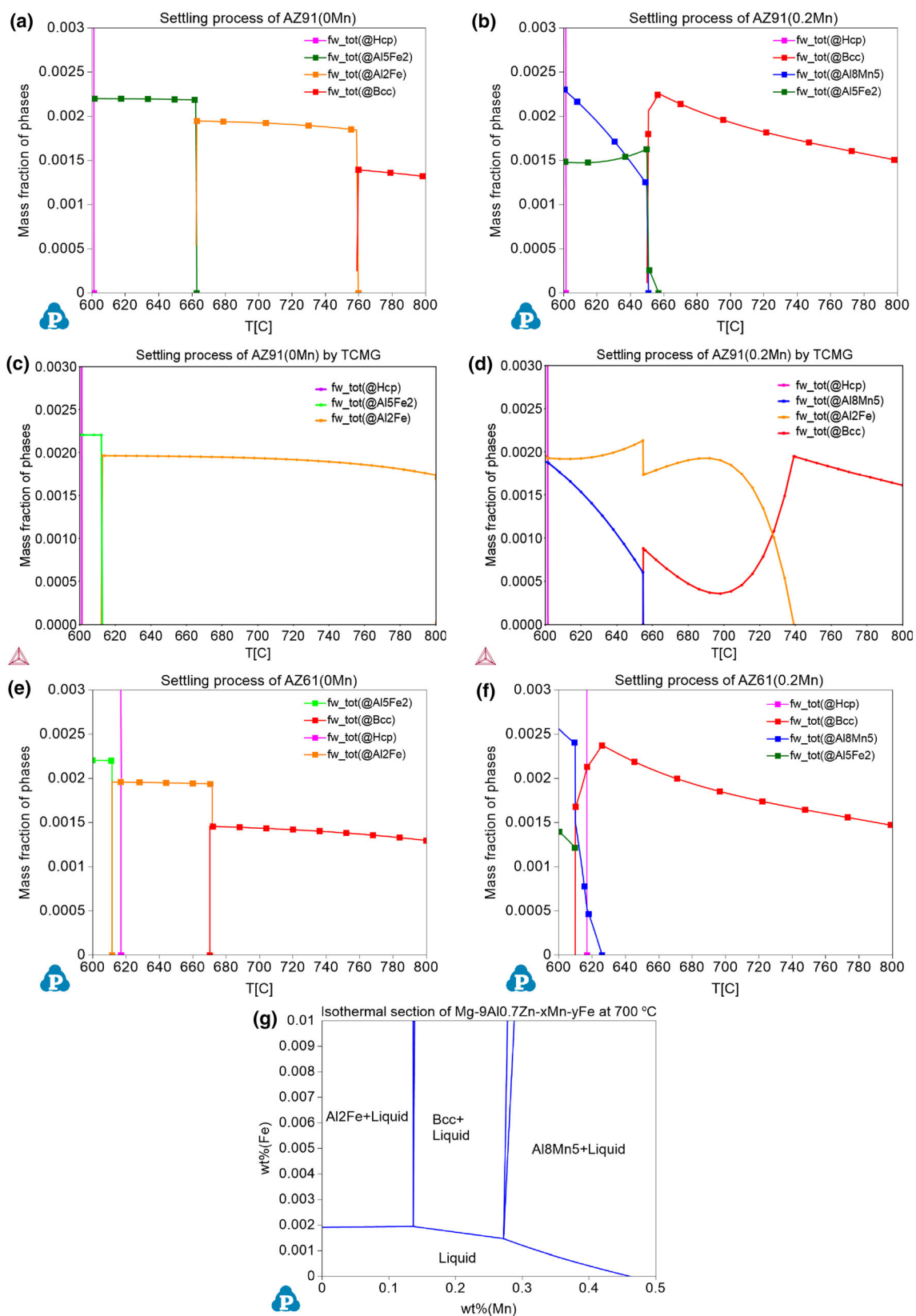


Fig. 2. Calculated equilibrium mass fractions of phases during the melting and settling process of alloys with an assumed initial contamination of 0.1 wt.% Fe: (a) AZ91(0Mn) using PanMg, (b) AZ91(0.2Mn) using PanMg, (c) AZ91(0Mn) using TCMG, (d) AZ91(0.2Mn) using TCMG, (e) AZ61(0Mn) using PanMg, (f) AZ61(0.2Mn) using PanMg, and (g) calculated isothermal section of Mg-9Al0.7Zn-xMn-yFe quaternary system at 700°C.

657°C. Under ideal equilibrium conditions, the initially assumed contamination of 1000 ppm Fe can be reduced to 8 ppm Fe in the liquid phase of AZ91(0.2Mn) at 660°C. It is also noted that, in the range 650–600°C, the first precipitate phase Al_5Fe_2 is replaced by a phase mixture of $\text{Al}_5\text{Fe}_2 + \text{Al}_8\text{Mn}_5$ by the addition of 0.2 wt.% Mn. The isothermal phase diagram section of AZ91 (Mg-9Al10.7Zn wt.%) with variation of Mn and Fe content at 700°C in Fig. 2g shows the two phases region Bcc + liquid where Mn addition is between 0.14 wt.% and 0.29 wt.% for a typical initial Fe contamination of 100 ppm Fe, as seen on the top edge of Fig. 2g.

As shown in Fig. 2a and b, during the settling process, there are four different precipitate phases, named Bcc(Fe, Al, Mn), Al_5Fe_2 , Al_2Fe , and Al_8Mn_5 , formed at different temperatures; they all contain significant Fe content. Al_8Mn_5 is modeled in PanMg with a complex sublattice structure, $(\text{Al})_{12}(\text{Mn})_5(\text{Al}, \text{Mn}, \text{Fe})_9$, and the significant solubility of Fe (around 20 wt.% Fe in some conditions) is predicted and

experimentally confirmed as shown in Table II. Recent details published by Zeng et al.⁴⁰ on this Al_8Mn_5 phase and its formation in AZ91 also confirmed the predictions in simulation calculations with PanMg. The composition of Bcc(Fe, Al, Mn) also varies, and the sequence of major components is reflected in the name. The Al_5Fe_2 and Al_2Fe compounds show only minor solubility ranges, which are nearly stoichiometric.

These phases were also observed in our experiments. Examples are shown in Fig. 3a and b and the results are noted in column “Exp. observed” of Table II. The density and the settling velocity of the second phases calculated by Stokes equation are listed in Table II. The same strategy can also be applied for the AZ61 alloy, as shown in Fig. 2e and f. The formation temperature of the high-density Fe-rich precipitate Bcc is reduced from about 670°C in the Mn-free AZ61 to about 610°C, with a maximum at 626°C by the addition of 0.2 wt.% Mn.

Table II. Precipitates from melt predicted and observed during the settling process

Alloy ^a	Settling temp. (°C)	Formed precipitates at the settling			Density (10^3 kg/ m^3)	v (10^{-5} m/s)	Ref. ^b
		PanMg calc.	TCMG calc.	Exp. observed			
AZ91 (0Mn)	700	Al_2Fe	Al_2Fe	Al_5Fe_2	4.0	6.5	This work
	660	Al_5Fe_2	Al_2Fe	Al_5Fe_2	4.0	5.9	
	620	Al_5Fe_2	Al_2Fe	Al_5Fe_2	4.0	5.1	
AZ91 (0.1Mn)	700	Al_2Fe	Al_2Fe	Bcc(Fe, Al, Mn)	5.6	11.0	
	660	Al_5Fe_2	Al_2Fe	$\text{Al}_5(\text{Fe}, \text{Mn})_2$	4.0	5.9	
AZ91 (0.2Mn)	700	Bcc	Bcc	Bcc(Fe, Al, Mn)	5.6	11.0	
			Al_2Fe	$\text{Al}_2(\text{Fe}, \text{Mn})$	4.0	6.2	
	660	Al_8Mn_5	Al_8Mn_5	$\text{Al}_8(\text{Mn}, \text{Fe})_5$	4.4	7.0	
		Al_8Mn_5	Al_2Fe	$\text{Al}_8(\text{Mn}, \text{Fe})_5$	4.4	6.0	
Mg-0.1Zr	700	Fe_2Zr	Fe_2Zr		7.7	16.6	
	Casted	Al_2Fe	Al_2Fe	Al_5Fe_2	4.0		44
Mg8Al0.025Fe	Casted	Al_2Fe	Al_2Fe	$\text{Al}_5(\text{Mn}, \text{Fe})_2$	4.0		
		(700°C)	(700°C)				
Mg4.2Al1.2Zn0.3Mn0.02Fe	Hot-deformed	Al_8Mn_5	Al_5Fe_2	$\text{Al}_8(\text{Mn}, \text{Fe})_5$			
		$\text{Al}_{13}\text{Fe}_4$	Al_8Mn_5				
Mg5Al1.1Zn0.68Mn0.025Fe	Casted	Al_8Mn_5	Al_8Mn_5	Bcc			
		(700°C)	(700°C)	Al_8Mn_5			
AZ61	650–690	Bcc	Bcc	Al_8Mn_5			18
		(670°C)	(670°C)				

^aInitial Fe-contamination of 200 ppm is taken for calculations, close to the experimental data of some 180 ppm Fe. ^bReferences for experimentally observed precipitates.

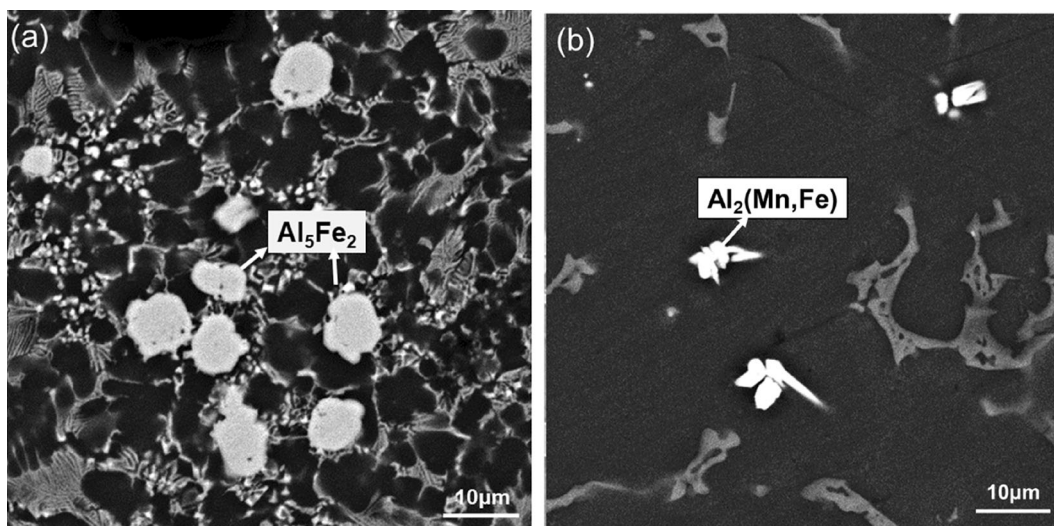


Fig. 3. BSE micrographs displaying Fe-rich particles from the bottom of the melt alloy: (a) Al_5Fe_2 in AZ91(0.2Mn) at 700°C; (b) $Al_2(Fe, Mn)$ in AZ91(0.2Mn) at 660°C.

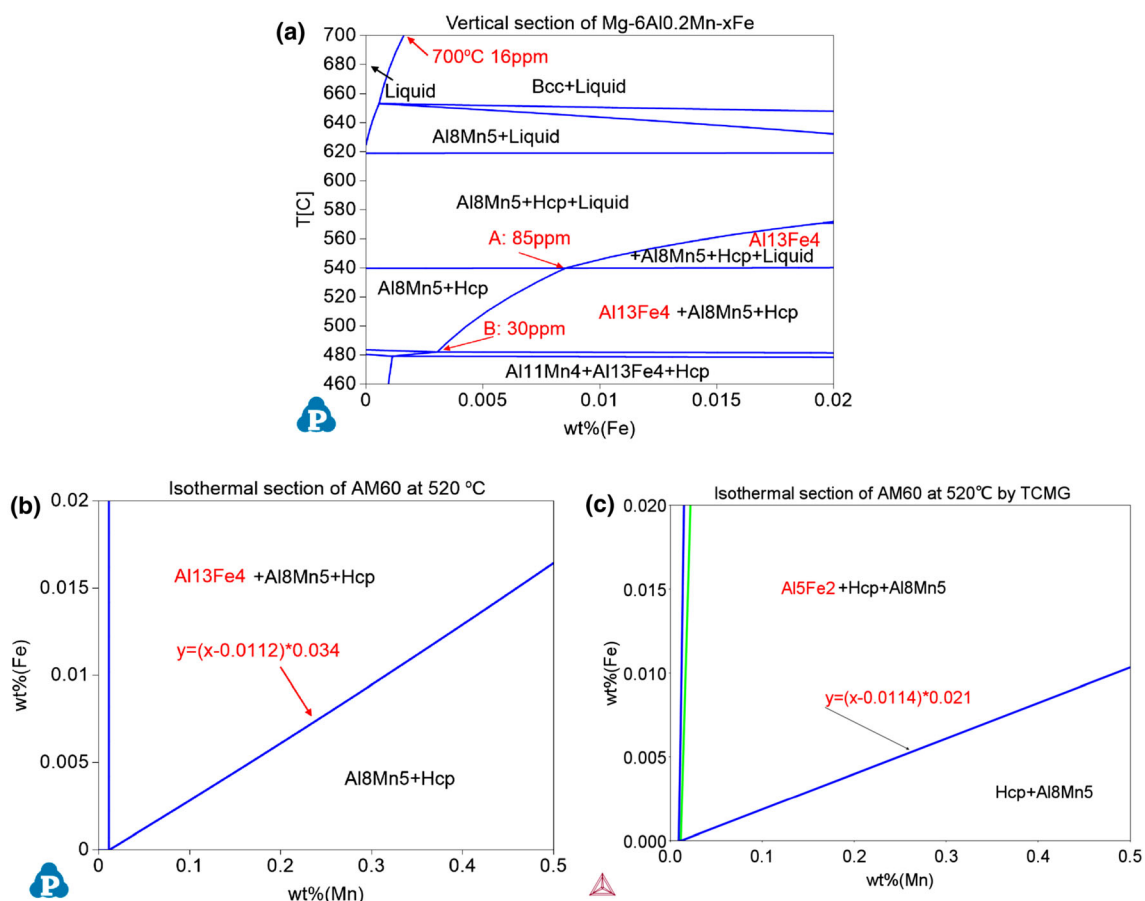


Fig. 4. (a) Calculated vertical section of AM60 with Fe addition, and calculated isothermal section of AM60 (Mg-6Al-xMn-yFe) at 520°C with varying content of Mn and Fe by (b) PanMg, and (c) TCMG.

Effect of Mn Addition on Fe Transformation in Solidification Process of AM Alloys

The analysis of various Fe content at constant 0.2 wt.% Mn in AM60 alloy starts with the calculated

equilibrium phase diagram section (isopleth) of AM60 (Mg-6Al0.2Mn-xFe wt.%) shown in Fig. 4. For typical iron contamination, the settling process at 700°C would ideally end with all the initial Bcc

particles settled, leaving a homogeneous liquid with 16 ppm Fe. In practice, settling is terminated prematurely in the two-phase region liquid + Bcc above 16 ppm Fe. Figure 4a reveals a narrow window for the at least part-transformation of Bcc to Al_8Mn_5 if, before casting, the temperature is reduced below about 650°C, but sensibly above 620°C, where massive crystallization of hexagonal close-packed(Mg) (Hcp(Mg)) would start. For the example of 50 ppm, residual Fe content in this transformation is completed at 649°C, leaving liquid + Al_8Mn_5 as the alloy to be cast. At this point, the Fe content of the liquid is further reduced to 5 ppm and the remaining Fe is dissolved in the Al_8Mn_5 phase with 18 wt.% Fe.

Even if casting is done directly from temperatures above 650°C, one may assume that the transformation to Al_8Mn_5 proceeds substantially for a moderate cooling rate, given the wide equilibrium freezing range of Hcp (Mg) from 620°C to 540°C. Under such conditions, the as-cast phase assembly may be approximately predicted by the phase regions just below the solidus in the phase diagram of Fig. 4a. These are the two-phase Al_8Mn_5 + Hcp and three-phase $\text{Al}_{13}\text{Fe}_4$ + Al_8Mn_5 + Hcp regions from 540°C to about 490°C.

Assuming an intermediate temperature of 520°C, safely below the solidus, the boundary between these two regions varies with the Mn content of the alloy, as shown in Fig. 4b and c. In Fig. 4b, the boundary between Al_8Mn_5 + Hcp and $\text{Al}_{13}\text{Fe}_4$ + Al_8Mn_5 + Hcp is at 60 ppm Fe for 0.2 wt.% Mn, consistent with Fig. 4a. This boundary is a straight line in Fig. 4b. It is the edge of the three-phase triangle $\text{Al}_{13}\text{Fe}_4$ + Al_8Mn_5 + Hcp, which is described by the equation $y = (x - 0.0112) \times 0.034$. The Mn content is usually in the 0.1–0.5 wt.% range, so we neglect the small offset of 0.0112 wt.% Mn, which provides the linear relationship $w(\text{Fe}) = 0.034 \times w(\text{Mn})$. The value of this slope of the phase boundary depends on the temperature chosen. For the isothermal section calculated at 500°C with PanMg the slope is $w(\text{Fe})/w(\text{Mn}) = 0.023$ instead of 0.034, as in Fig. 4b for 520°C. Similar values are obtained by calculating with the TCMG database (see Fig. 4c).

Effect of Mn Addition on Fe Transformation in Solidification Process of AZ Alloys

The phase diagram section of AZ91 (Mg-9Al0.7Zn0.2Mn) with variation of Fe content is shown in Fig. 5a. A calculation along a line of constant 100 ppm Fe in Fig. 5 reveals that Al_8Mn_5 dissolves some 21 wt.% Fe at the beginning of precipitation, decreasing to 3.2 wt.% Fe at 545°C where its mass fraction has grown to $f(\text{Al}_8\text{Mn}_5) = 0.0031$. That means that almost all of the 100 ppm Fe are now bonded in this solution phase, sharing the sublattice with the majority component Mn. At 508°C, the end of the four-phase region,

$\text{Al}_{13}\text{Fe}_4$ + Al_8Mn_5 + Hcp + liquid in Fig. 5b, $\text{Al}_{13}\text{Fe}_4$ carries 60 ppm Fe, while Al_8Mn_5 has 40 ppm Fe. In the five-phase reaction at 507°C, the Al_8Mn_5 transforms to $\text{Al}_{11}\text{Mn}_4$, which carries virtually no Fe. The 40-ppm Fe is taken up by an increasing amount of the $\text{Al}_{13}\text{Fe}_4$ phase. At this point, all the Fe is bounded in this almost stoichiometric $\text{Al}_{13}\text{Fe}_4$ phase.

Between 482 and 463°C, $\text{Al}_{13}\text{Fe}_4$ and $\text{Al}_{11}\text{Mn}_4$ transform completely, under equilibrium conditions, to Al_4Mn , with final $f(\text{Al}_{11}\text{Mn}_4) = 0.0062$ and 1.6 wt.% Fe. Again, all the 100 ppm Fe is in the solution phase, $\text{Al}_{11}\text{Mn}_4$. A major distinction of Fig. 5a compared to the phase diagram for the Zn-free alloy AM60 in Fig. 4a is the much lower solidus, 463°C for AZ91 compared to 540°C for AM60. In a real mold casting scenario, it is unlikely that all the equilibrium transformations proceed, especially those two at the end. These are at 507°C (Al_8Mn_5 to $\text{Al}_{11}\text{Mn}_4$) and below 482°C ($\text{Al}_{13}\text{Fe}_4$ and $\text{Al}_{11}\text{Mn}_4$ to Al_4Mn). Therefore, we take a closer look at a critical phase above 507°C, point C in Fig. 5a, and below 507°C, point D in Fig. 5a. This region is magnified in Fig. 5b.

Starting from point C (40 ppm Fe, 507.5°C) at a higher temperature, the critical phase boundary separates the region Al_8Mn_5 + Hcp(Mg) + liquid from $\text{Al}_{13}\text{Fe}_4$ + Al_8Mn_5 + Hcp(Mg) + liquid. Alloys in the latter region with more than 40 ppm Fe are prone to form the secondary phase $\text{Al}_{13}\text{Fe}_4$, which deteriorates the corrosion resistance property. Starting at point D (13 ppm Fe, 507.1°C) at a lower temperature, the critical phase boundary separates the region $\text{Al}_{11}\text{Mn}_4$ + Hcp(Mg) + liquid from $\text{Al}_{13}\text{Fe}_4$ + $\text{Al}_{11}\text{Mn}_4$ + Hcp(Mg) + liquid.

From Fig. 5b, we can only see the critical Fe content at constant 0.2 wt.% Mn. In analogy to the approach given in Fig. 4b and c, the dependence of the critical Fe content on Mn content is obtained from the isothermal sections. The temperatures are selected just above point C at 510°C and just below point D at 505°C with the same constant 9 wt.% Al and 0.7 wt.% Zn, and the phase diagram sections are given in Fig. 5c and d.

At 510°C in Fig. 5c, the critical phase boundary separating $\text{Al}_{13}\text{Fe}_4$ + Al_8Mn_5 + Hcp(Mg) + liquid from Al_8Mn_5 + Hcp(Mg) + liquid develops into a straight line. The slope is $w(\text{Fe})/w(\text{Mn}) = 0.023$, while at 520°C, the slope is larger, $w(\text{Fe})/w(\text{Mn}) = 0.030$. At 505°C in Fig. 5d, the critical phase boundary separating $\text{Al}_{13}\text{Fe}_4$ + $\text{Al}_{11}\text{Mn}_4$ + Hcp(Mg) + liquid from $\text{Al}_{11}\text{Mn}_4$ + Hcp(Mg) + liquid is a straight line, with the slope $w(\text{Fe})/w(\text{Mn}) = 0.007$. This is much below the experimental value and suggests that the five-phase reaction at 507°C where Al_8Mn_5 should transform to $\text{Al}_{11}\text{Mn}_4$ may indeed not proceed under real casting conditions. This is essentially a solid-state reaction because the small mass fraction of the liquid changes only a little. At 510°C $f(\text{liquid}) = 0.14$ and at 505°C $f(\text{liquid}) = 0.12$, these values are independent of the Fe

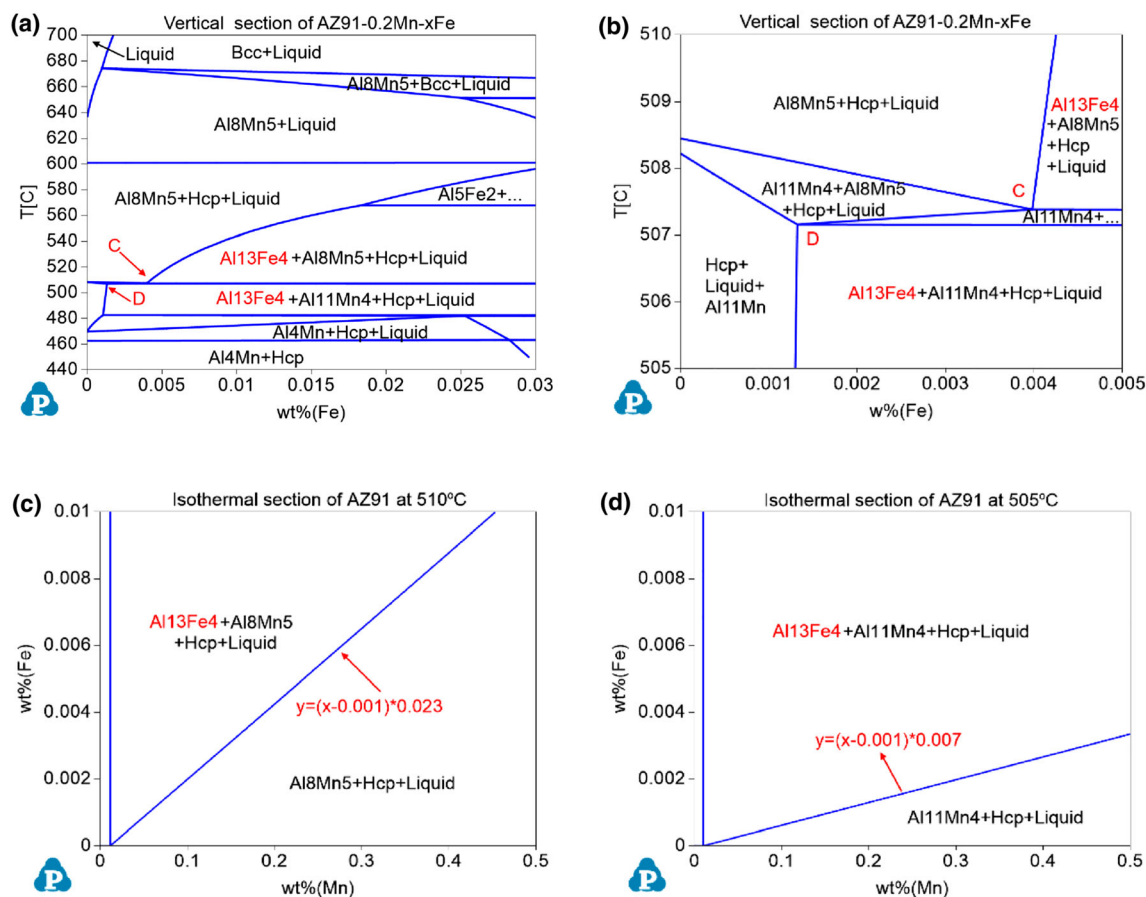


Fig. 5. Calculated vertical sections of AZ91 with addition of Fe (Mg-9Al0.7Zn0.2Mn-xFe), (a) up to 300 ppm Fe and (b) magnification around points C and D up to 50 ppm Fe; and calculated isothermal sections with varying content of Mn and Fe in "AZ91" (Mg-9Al0.7Zn-xMn-yFe), (c) at 510°C and (d) at 505°C.

Table III. Precipitates predicted and observed in AM and AZ alloys

Alloy ^a (wt.%)	Casting type	Precipitates predicted, equilibrium calc. at 520°C			Ref. ^b
		PanMg	TCMG	Precipitates observed	
AM50	Die cast	Al ₈ Mn ₅ Al ₁₃ Fe ₄	Al ₈ Mn ₅ Al ₅ Fe ₂	Al ₁₂ Mg ₁₇ , Al ₈ Mn ₅	45
AM50	Cast	Al ₈ Mn ₅ Al ₁₃ Fe ₄	Al ₈ Mn ₅ Al ₅ Fe ₂	Al-Mn-Fe IMCs	16
AM60	Cast	Al ₈ Mn ₅ Al ₁₃ Fe ₄	Al ₈ Mn ₅ Al ₅ Fe ₂	Al-Mn-Fe IMCs	16
AZ31	Solidified	Al ₈ Mn ₅ Al ₅ Fe ₂	Al ₈ Mn ₅ Al ₅ Fe ₂	Al _{0.89} Mn _{1.11} Al ₈ (Mn, Fe) ₅	41
AZ63	Solidified	Al ₁₃ Fe ₄ Al ₈ Mn ₅	Al ₈ Mn ₅ Al ₅ Fe ₂	Al ₈ (Mn, Fe) ₅	41

^aCompositions assumed for calculations: AM50 (Mg-5Al0.2Mn), AM60 (Mg-6Al0.2Mn), AZ31(Mg-3Al0.7Zn0.2Mn), AZ63 (Mg-6Al3Zn0.2Mn), with initial 200 ppm Fe. ^bReferences for experimentally observed precipitates.

content shown in Fig. 5a. Additional support may come from the fact that the commonly observed precipitations in the AZ63 and AZ31 alloys are mainly Al_8Mn_5 ,⁴¹ as compiled in Table III. That is closer to the phase relationships shown in Fig. 5c, with Al_8Mn_5 instead of $\text{Al}_{11}\text{Mn}_4$ in Fig. 5d. Thus, the phase boundary in Fig. 5d may not be relevant.

DISCUSSION

Effect of Mn Addition on the Purification of Mg-(Fe) and Mg-Al-X Alloys

As described in “Effect of Mn Addition on the Fe Distribution in Mg-(Fe) Melts” and “Effect of Mn Addition on the Fe Distribution in Mg-Al-(Fe) Melts” sections, the thermodynamics of the system, e.g., the relationship of the joint solubility of Fe and Mn in liquid Mg and the phase transformation information, can effectively guide the amount of Mn addition in Mg melt for purification. Firstly, both the calculated and experimental results show that Mn addition distinctly reduces the Fe solubility in Mg-rich melt due to the formation of Fe-Mn-(Al) compounds. Secondly, the efficiency of the settling process, that is, the percent of the settled precipitates, is dependent on the dynamics of the settlement of the ‘precipitates, where the types of the precipitates are controlled by the alloy composition and settling temperature. Thirdly, low settling and casting temperatures are also always suggested for low corrosion rates of Mg alloys, where the final state and distribution impurities can change the rate of the micro-galvanic corrosion.

At the settling temperature, it is assumed that the equilibrium liquid + “primary-precipitate” is attained so that the liquid composition follows the solubility line in Figs. 1c and 2g for any combination of initial Fe and Mn content above that line. In the ideal case, all the primary-precipitates settle down leaving the homogeneous saturated liquid behind, which then becomes the overall composition of the cast alloys. The reason of the reduction of Fe content is mainly attributed to the decrement of Fe solubility in Mg alloys with Mn addition.

It is observed that the Mn addition also controls the type of the ‘precipitate phase. With respect to the Mg-(Mn, Fe) alloy, for the Cbcc(Mn, Fe) precipitate phase, Mn is the majority component with minor Fe in contrast to Fcc(Fe, Mn) phase, where Fe is the majority component with minor Mn as detailed in Table I. It is reported that Cbcc(Mn, Fe) is less detrimental for the galvanic corrosion in Mg alloy compared to Fcc(Fe, Mn) phase.⁴² That is important because the residual Fe content left after the purification even with perfect settling stage in the homogeneous saturated liquid must transform during casting in eutectic reaction also

into the precipitates Bcc, Fcc(Fe, Mn) and Cbcc(Mn, Fe).

With respect to the Mg-Al-X alloy, any additional Fe in the alloy is chemically bonded in the precipitates, like Al_5Fe_2 , Al_2Fe , Bcc(Fe, Al, Mn), and $\text{Al}_8(\text{Mn, Fe})_5$, depending on the settling temperature and the amount of Mn addition. As shown in Table II and Fig. 2, the addition of Mn changes the type of precipitated phase with significant effects on the efficiency of the settling process. For example, as shown in Table II, the terminal settling velocity of the precipitate Al_2Fe in AZ91(0Mn) at 700°C is around 6.5×10^{-5} m/s. For simplicity, assuming a height of the furnace of 1 m, the time required for a precipitate on the top to reach the bottom is 1.5×10^4 s (~ 4.2 h). This value is much longer than the usually applied industrial settling time (1/2 h), chosen as a compromise between melt quality and process cost. Clearly, the efficiency and effectiveness of the settling process is actually one of the determining factors of the final purity of the alloy. With 0.1 wt.% Mn addition to the AZ91 alloy, the high-density precipitate Bcc forms at 700°C, the terminal settling velocity of Bcc is then 1.7 times higher compared to that of Al_5Fe_2 in Mn-free AZ91, as shown in Table II. The calculated terminal settling velocity of Fe_2Zr would be even higher if the Fe_2Zr precipitate forms in the Mg melt with a Zr additive. However, for the Mg-Al-X series alloy, added Zr can react with Al and form Al-Zr compounds without extracting excess Fe. Hence, Zr is not applicable for the purification of Mg-Al-X alloys. Thus, the Mn purification effect of AZ alloys is optimized by the formation of suitable Bcc precipitates at a lower temperature, enhancing the efficiency of the settling process. Since the current commercial settling process temperature is around 700–730°C, the isothermal phase diagram section of alloys with variations of Mn and Fe content at 700°C can then effectively guide the choice of Mn addition. As described in “Effect of Mn Addition on the Fe Distribution in Mg-Al-(Fe) Melts” section, it is suggested to aim at the formation of Bcc as the high-density and high-Fe content precipitate for the settling process; that is, to achieve in the two phases Bcc + liquid region.

Low settling and casting temperatures have also recently been suggested for low corrosion rates of Mg alloys.¹⁸ Firstly, the solubility of iron in the liquid is reduced at low temperature, enabling a theoretically lower remaining Fe content in the liquid, i.e., in the alloy after complete settling. Secondly, at a lower temperature before casting, the second phase particles with low Fe content may be preferentially formed, which have less harmful effects¹⁶ on galvanic corrosion compared to Fe-rich precipitates Bcc. Liu and Song⁸ also suggested that

there is a critical temperature range for the casting of Mg-Al-Mn-X (AXJ530 in their work) in order to form only the relatively passive phase, Al_8Mn_5 , as opposed to the Fe-rich Bcc phase, which is much more harmful for the corrosion property of Mg alloys.

Effect of Mn Addition on the Tolerance of Fe in AM and AZ Alloys

The corrosion tolerance limit of Fe with Mn content in AM and AZ Mg alloys was experimentally observed and found to depend on the Fe/Mn mass ratio; the values mostly reported in the literature are $w(\text{Fe})/w(\text{Mn}) \approx 0.032$ for AZ91 and $w(\text{Fe})/w(\text{Mn}) \approx 0.021$ for AM60.^{14,26–30} These experimental data, especially the work by Hillis and Reichek, have been analyzed by Liu et al.⁴³ who also showed that the calculated phase diagrams are a powerful tool to predict critical casting temperature limits to avoid the formation of the harmful Bcc phase. As described in “Effect of Mn Addition on Fe Transformation in Solidification Process of AM Alloys” and “Effect of Mn Addition on Fe Transformation in Solidification Process of AZ Alloys” sections, the values reported for critical Fe/Mn ratios can be effectively predicted by thermodynamic equilibrium calculations. It is shown the tolerance limit of Fe depending on Mn content is correlated with the boundary between the region with an active phase and the region without an active phase. Here, the intermetallic compound (IMC) with dissolved Fe is less active compared to Fe as the main component, regarding to the galvanic corrosion.

With respect to the AM60 alloy, the tolerance limit of Fe depending on Mn content is correlated with the region boundary between $\text{Al}_8\text{Mn}_5 + \text{Hcp}$ and $\text{Al}_{13}\text{Fe}_4 + \text{Al}_8\text{Mn}_5 + \text{Hcp}$, because Fe is dissolved in the Al_8Mn_5 phase in a sublattice together with Mn as opposed to the stoichiometric phase $\text{Al}_{13}\text{Fe}_4$. That is a qualitative distinction where the IMCs below that boundary may be less harmful for corrosion. The calculated boundary line between $\text{Al}_8\text{Mn}_5 + \text{Hcp}$ and $\text{Al}_{13}\text{Fe}_4 + \text{Al}_8\text{Mn}_5 + \text{Hcp}$ with the slope as $w(\text{Fe})/w(\text{Mn}) = 0.034$ or 0.021 (at 520°C calculated using PanMg or TCMG) is quite close to the tolerance limit of $w(\text{Fe})/w(\text{Mn}) \approx 0.021$ reported in the literature.^{14,26–30}

The present analysis for AM60 has been extended to other alloys and the results are summarized in Table III. The type of the precipitates in the final solidified alloy was calculated using PanMg and TCMG databases for the chosen equilibrium temperature of 520°C , as explained above, and compared to experimental observations. It is noted that only in the first alloy, AM50, is the $\text{Al}_{12}\text{Mg}_{17}$ precipitates observed, which is ascribed to the much higher cooling rate in this die-cast alloy. This occurrence of $\text{Al}_{12}\text{Mg}_{17}$ is also predicted for thermodynamic simulation under Scheil conditions. For all other alloys in Table III, a reasonable agreement is

obtained between the predictions calculated under equilibrium conditions with two different databases and experimental observations.

For the AZ series alloys, the commercial alloy AZ91 has been taken for analysis. As shown in “Effect of Mn Addition on Fe Transformation in Solidification Process of AZ Alloys” section, the calculated phase boundary line separating $\text{Al}_{13}\text{Fe}_4 + \text{Al}_8\text{Mn}_5 + \text{Hcp}(\text{Mg}) + \text{liquid}$ from $\text{Al}_8\text{Mn}_5 + \text{Hcp}(\text{Mg}) + \text{liquid}$ at 510°C is with the slope $w(\text{Fe})/w(\text{Mn}) = 0.023$, while at 520°C the slope $w(\text{Fe})/w(\text{Mn}) = 0.030$. That slope, of course, depends on the temperature selected for the isothermal section. Despite all the approximations made, this is not too far from the tolerance limit of $w(\text{Fe})/w(\text{Mn}) \approx 0.032$ reported in the literature.²⁷

CONCLUSION

Purification of the melt can reduce an initial Fe contamination by the settling of Fe-containing solid phases, and can be controlled by proper selection of the settling temperature and added Mn content. Thermodynamic calculations demonstrate that the temperature, ranging from some 700°C down to just above the massive crystallization of Hcp(Mg) phase, has a strong impact on the type of precipitate forming being essentially isothermal in the melt. Evaluation of settling velocities demonstrates that incomplete settling, prematurely terminated after practical settling times, must also be realistically assumed for the particles in other Mg-Al-based alloys. The results of the thermodynamic calculations can guide the settling temperature to either aim at an Al_8Mn_5 phase or at a high-density Fe-rich phase for quick settling.

The tolerance of Fe in cast alloys is strongly related to the Al_8Mn_5 phase, which is a complex intermetallic phase dissolving Fe on the same sublattice jointly with Mn, modeled as $(\text{Al})_{12}(\text{Mn})_5(\text{Al}, \text{Mn}, \text{Fe})_9$. The phase diagram calculations near the solidus temperature of the AM and AZ alloys reveal that a key phase boundary can be identified separating it from the (more Fe-rich) region where the detrimental $\text{Al}_{13}\text{Fe}_4$ phase occurs in addition. This phase boundary shows a linear relationship between the Fe and Mn content and, thus, an approximately constant Fe/Mn ratio. This $w(\text{Fe})/w(\text{Mn})$ ratio is not too far off the experimentally reported corrosion tolerance limit of Fe with Mn content in AM and AZ Mg alloys.

ACKNOWLEDGEMENTS

The authors are grateful for the financial supports from National Natural Science Foundation of China (51971044 and U1910213), Natural Science Foundation of Chongqing (cstc2019yszx-jcyjX0004 and cstc2018jcyjAX0070), Qinghai Provincial Science and Technology Key Program (No. 2018-GX-A1), National Key Research and Development Program of China (2016YFB0301102) and Fundamen-

tal Research Funds for the Central Universities (2019CDJGFCL005 and 2020CDJDPT001). A fellowship from the Karlsruhe Institute of Technology for the research guest stay of author Prof. Yuan Yuan during preparation of this manuscript is greatly acknowledged.

CONFLICT OF INTEREST STATEMENT

On behalf of all authors, the corresponding author states that there is no conflict of interest.

SUPPLEMENTARY MATERIAL

The online version of this article (<https://doi.org/10.1007/s11837-020-04550-5>) contains supplementary material, which is available to authorized users.

REFERENCES

1. T.B. Abbott, *Corrosion* 71, 120 (2015).
2. W.J. Joost and P.E. Krajewski, *Scr. Mater.* 128, 107 (2017).
3. S. You, Y. Huang, K.U. Kainer, and N. Hort, *J. Magnes. Alloy* 5, 239 (2017).
4. J.P. Weiler, *J. Magnes. Alloy* 7, 297 (2019).
5. J. Song, J. She, D. Chen, and F. Pan, *J. Magnes. Alloy* 8, 1 (2020).
6. A. Atrens, G. Song, M. Liu, Z. Shi, F. Cao, and M.S. Dargusch, *Adv. Eng. Mater.* 17, 400 (2015).
7. M. Esmaily, J.E. Svensson, S. Fajardo, N. Birbilis, G.S. Frankel, S. Virtanen, R. Arrabal, S. Thomas, and L.G. Johansson, *Prog. Mater. Sci.* 89, 92 (2017).
8. M. Liu and G. Song, *Corros. Sci.* 77, 143 (2013).
9. K. Gusieva, C. Davies, J. Scully, and N. Birbilis, *Int. Mater. Rev.* 60, 169 (2015).
10. T. Morishige, K. Ueno, M. Okano, T. Goto, E. Nakamura, and T. Takenaka, *Mater. Trans.* 55, 1506 (2014).
11. Z. Qiao, Z. Shi, N. Hort, N.I. Zainal Abidin, and A. Atrens, *Corros. Sci.* 61, 185 (2012).
12. H. Gao, G. Wu, W. Ding, L. Liu, X. Zeng, and Y. Zhu, *Mater. Sci. Eng., A* 368, 311 (2004).
13. G. Wu, H. Gao, W. Ding, and Y. Zhu, *J. Mater. Sci.* 40, 6175 (2005).
14. M. Liu, P. Uggowitzer, P. Schmutz, and A. Atrens, *JOM* 60, 39 (2008).
15. G.T. Parthiban, N. Palaniswamy, and V. Sivan, *Anti-corros. Meth. Mater.* 56, 79 (2009).
16. H. Matsubara, Y. Ichige, K. Fujita, H. Nishiyama, and K. Hodouchi, *Corros. Sci.* 66, 79 (2013).
17. N. Birbilis, G. Williams, K. Gusieva, A. Samaniego, M.A. Gibson, and H.N. McMurray, *Electrochem. Commun.* 34, 295 (2013).
18. F. Pan, X. Chen, T. Yan, T. Liu, J. Mao, W. Luo, Q. Wang, J. Peng, A. Tang, and B. Jiang, *J. Magnes. Alloy* 4, 8 (2016).
19. G. Wu, M. Sun, W. Wang, and W. Ding, *Chin. J. Nonferrous Metals*. 20, 1021 (2010).
20. A. Prasad, P.J. Uggowitzer, Z. Shi, and A. Atrens, *Adv. Eng. Mater.* 14, 477 (2012).
21. T. Chen, X. Xiong, Y. Yuan, A. Tang, D. Li, A. Atrens, and F. Pan, *Adv. Eng. Mater.* 8, 8 (2020).
22. C. Scharf and A. Ditze, *Adv. Eng. Mater.* 9, 566 (2007).
23. X. Chen, F. Pan, J. Mao, and J. Huang, *J. Mater. Sci.* 47, 514 (2011).
24. D.S. Gandel, M.A. Easton, M.A. Gibson, T. Abbott, and N. Birbilis, *Corros. Sci.* 81, 27 (2014).
25. D. Gandel, N. Birbilis, M. Easton, and M. Gibson, Influence of manganese, zirconium and iron on the corrosion of magnesium, *Proceedings of corrosion prevention 2010*, Adelaide, Australia, 2010.
26. J.E. Hillis, *SAE*, 830523 (1983).
27. K.N. Reichek, K.J. Clark, and J.E. Hillis, *SAE*, 850417 (1985).
28. J.E. Hillis and K.N. Reichek, *SAE*, 860288 (1986).
29. J.E. Hillis and S.O. Shook, *SAE*, 890205 (1989).
30. W.E. Mercer and J.E. Hillis, *SAE*, 920073 (1992).
31. R. Schmid-Fetzer, *J. Phase Equilib. Diff.* 35, 735 (2014).
32. R. Shi and A.A. Luo, *Calphad* 62, 1 (2018).
33. R. Schmid-Fetzer and F. Zhang, *Calphad* 61, 246 (2018).
34. Y. Yuan, The Integrated Alloy Design of Anti-corrosion Magnesium Alloy, *TMS 2020*, 149th Annual Meeting & Exhibition, San Diego, California, USA, 2020.
35. A.R. Natarajan and A. Van der Ven, *Phys. Rev. B*, 95 (2017).
36. A. Van der Ven, J.C. Thomas, B. Puchala, and A.R. Natarajan, *Annu. Rev. Mater. Res.* 48, 27 (2018).
37. L. Tian and W. Yu, *Comp. Mater. Sci.*, 186 (2021).
38. J.O. Andersson, T. Helander, L. Höglund, and P. Shi, *Calphad* 26, 273 (2002).
39. V. Mitrovic-Scepanovic, R.H. Packwood, G.J.C. Carpenter, and R.J. Brigham, *Can. Metall. Q.* 33, 61 (1994).
40. L. Peng, G. Zeng, T.C. Su, H. Yasuda, K. Nogita, and C.M. Gourlay, *JOM* 71, 2235 (2019).
41. G. Han and X. Liu, *Acta Mater.* 114, 54 (2016).
42. D.S. Gandel, M.A. Easton, M.A. Gibson, and N. Birbilis, *Corrosion* 69, 744 (2013).
43. M. Liu, P.J. Uggowitzer, A.V. Nagasekhar, P. Schmutz, M. Easton, G. Song, and A. Atrens, *Corros. Sci.* 51, 602 (2009).
44. E.F. Volkova, *Metal. Sci. Heat Treat.* 59, 154 (2017).
45. R.M. Wang, A. Eliezer, and E.M. Gutman, *Mater. Sci. Eng. A* 355, 201 (2003).

Publisher's Note Springer Nature remains neutral with regard to jurisdictional claims in published maps and institutional affiliations.